

## Article

# Mechanical and Tribological Properties of the CrAl/CrAlN and CrAl/CrAlN-(a-CN<sub>x</sub>) Multilayers Deposited by HIPIMS

Cecilio J. Martínez-González <sup>1,2</sup>, Max F. Flores-Jiménez <sup>3</sup>, David I. Bravo-Barcenas <sup>3</sup>, Omar Jiménez-Alemán <sup>4</sup>  
and Martín Flores-Martínez <sup>4,\*</sup>

<sup>1</sup> Centro Universitario de Ciencias Exactas e Ingenierías (CUCEI), Universidad de Guadalajara, Blvd. Marcelino García Barragán 1421, Olímpica, Guadalajara 44430, Mexico; cecilio.martinez9250@alumnos.udg.mx

<sup>2</sup> Programa de Maestría en Ciencia e Ingeniería de Los Materiales, Quantum-Ciudad del Conocimiento, Universidad Autónoma de Zacatecas, Av. Marie Curie, 1000 Blv. El Bote, Col. Ciudad Argentum Zacatecas, Zacatecas 98047, Mexico

<sup>3</sup> Centro Universitario de Ciencias Exactas e Ingenierías (CUCEI), CONACyT-Universidad de Guadalajara, Boulevard Marcelino García Barragán 1421, Guadalajara 44430, Mexico; max.flores@academicos.udg.mx (M.F.F.-J.); david.bravo@academicos.udg.mx (D.I.B.-B.)

<sup>4</sup> Departamento de Ingeniería de Proyectos, Centro Universitario de Ciencias Exactas e Ingenierías (CUCEI), Universidad de Guadalajara, Blvd. Marcelino García Barragán 1421, Olímpica, Guadalajara 44430, Mexico; omar.aleman@academicos.udg.mx

\* Correspondence: martin.fmartinez@academicos.udg.mx

**Abstract:** In this study, two CrAl/CrAlN multilayer coatings of 1.5 μm and 1.2 μm thicknesses were deposited from a (50:50) CrAl sectioned target by high-power impulse magnetron sputtering (HIPIMS) onto A11 tool steel to evaluate the effect over mechanical and tribological properties by the addition of an (a-CN<sub>x</sub>) top layer. XRD analysis showed a CrAlN FCC structure (111) and a Cr phase (110). A glass-like morphology was observed in the CrAl layer and in the (a-CN<sub>x</sub>) top layer, while the CrAlN layers exhibited a columnar morphology according to the FE-SEM analysis. Raman analysis results confirmed characteristic peaks G and D for the carbon amorphous structure of the (a-CN<sub>x</sub>) top layer. Nanoindentation results showed comparable hardnesses (23.08 GPa ± 2.8 and 20.58 GPa ± 1.8) in both multilayer coatings. The CrAl/CrAlN multilayer with an (a-CN<sub>x</sub>) top layer increased the absorption energy capacity and the mechanical potential energy stored. The nano scratch test showed the strongest crack resistance and highest adhesive energy values for the CrAl/CrAlN multilayer. The addition of an (a-CN<sub>x</sub>) top layer improved the tribological behavior when higher normal loads were applied during the fretting test. Raman analysis showed an increase in the I(D)/I(G) ratio and a formation of a carbon sp<sup>2</sup> structure (i.e., graphite-like structure) over the worn surfaces, as well as dissipated energy (J/m) during the fretting test.

**Keywords:** HIPIMS; nanoindentation; nano-scratch; fretting; chromium aluminum; carbon nitride



**Citation:** Martínez-González, C.J.; Flores-Jiménez, M.F.; Bravo-Barcenas, D.I.; Jiménez-Alemán, O.; Flores-Martínez, M. Mechanical and Tribological Properties of the CrAl/CrAlN and CrAl/CrAlN-(a-CN<sub>x</sub>) Multilayers Deposited by HIPIMS. *Coatings* **2023**, *13*, 1344. <https://doi.org/10.3390/coatings13081344>

Academic Editor: Elena Villa

Received: 12 July 2023

Revised: 25 July 2023

Accepted: 26 July 2023

Published: 31 July 2023



**Copyright:** © 2023 by the authors. Licensee MDPI, Basel, Switzerland. This article is an open access article distributed under the terms and conditions of the Creative Commons Attribution (CC BY) license (<https://creativecommons.org/licenses/by/4.0/>).

## 1. Introduction

Nowadays, industrial applications such as milling, turning steel, and high-speed cutting need tools coated with hard films to overcome the problems associated with high temperatures, oxidation, and corrosive environments, as well as to extend the service life of these industrial tools. In the past two decades some PVD free of Ti has been studied [1], the CrN-based form is well known for a superior wear and corrosion resistance and tenacity when compared to TiN. However, the CrN films have low hardness and are greatly restricted to engineering applications as engine parts, gears, shafts, and applications in metal forming and plastic molding operations [2]. On the other hand, it is well known that CrN and metal nitrides deposited by DC magnetron sputtering have a columnar structure, which is a disadvantage for some mechanical properties [3]. Alloying CrN films with another metal to form a ternary system has been widely studied to overcome this problem.

The new ternary film structure has a decreased grain size to that of the formation of different morphologies between phases. In the same way as a TiAlN system, the Al addition in the CrN cubic structure increases the hardness in the CrAlN films [4]. It has been observed that increasing the Al content in CrAlN systems improves its structure and thermal stability. Fabrication of CrAlN nanocomposite films deposited by magnetron sputtering from Cr and Al targets showed smaller grain size, higher hardness, and better wear resistance compared to CrN films [2]. Thin films deposited with DC balanced magnetron sputtering with a Cr/Al (30/70 at%) alloy target exhibited a moderated hardness, and a mixed structure of fcc-CrN and hcp-AlN was observed, but these films have poor mechanical properties [5]. However, using pulsed DC reactive sputtering technique films obtained at different pulse widths and a relation of 50/50 at% in the Cr/Al target, films with great microstructure and mechanical properties were obtained [6]. In other studies, CrAlN layers obtained with one Cr/Al (75/25 at%) or two targets (Cr and Al) deposited by magnetron sputtering showed well-crystallized and adhered films, and the film synthesized with one homogeneous target showed a relative low friction coefficient (0.31) and a columnar morphology; however, those made with two targets had a greater control over the chemical composition, a dense morphology, a higher hardness, and an improved Young's modulus [7]. A multilayer architecture is suggested to enhance the mechanical and tribological properties, as well as fracture toughness [8]. In some studies involving a CrAl/CrAlN multilayer coating deposited by the magnetron co-sputtering pulsed DC method with a target Cr/Al (0.25:0.75) area ratio, the results showed compressive stress when the bilayer period was reduced [9]. In other studies, when the CrN/CrAlN multilayer was deposited by RF-magnetron sputtering, mechanical properties showed superior hardness, high compressive stress, and plastic deformation resistance compared to the CrN monolayer [10].

In the last years, researchers have investigated the structure and properties of CrN-based films deposited through high-power impulse magnetron sputtering (HIPIMS), owing to their high density in comparison to other PVD techniques [11], obtaining coatings with a refined structure and lower residual stresses, higher hardness, and a change in the crystal orientation for the grown films [3,12]. Some studies determined that a N<sub>2</sub>/Ar ratio (>40%) is related to the FCC phase and that bias voltage has an influence over residual stress when CrAlN films are deposited from the Cr/Al (50/50 at%) target by HIPIMS [3]. However, tribological properties of the CrAlN multilayer could be degraded when it is exposed to cutting fluid environments due to AlN phase reaction under water lubrication accelerating the corrosion wear [13,14]. To overcome these problems, other studies proposed a CrAlN/CN<sub>x</sub> multilayer combining the high hardness and self-lubrication of CrAlN and CN<sub>x</sub> phases, respectively [15], as well as ensuring the good adhesion between CrAlN and CN<sub>x</sub> phases due to the Cr as a transition metal [16]. Some studies were directed to improve the adhesion of (a-CN<sub>x</sub>) films deposited by HIPIMS [17]. Other studies analyzed the wear resistance of (a-CN<sub>x</sub>) films deposited by HIPIMS and DC magnetron sputtering [18]. Moreover, in others, there was a comparison of the macro and micro tribological properties of (a-CN<sub>x</sub>) films deposited by HIPIMS [19]. Investigations regarding metallic/ceramic multilayer coatings deposited from sectioned targets showed the possibility of obtaining a multilayer CrAl/CrAlN deposited from a Cr: 0.25 and Al: 0.75 area ratio by the magnetron co-sputtering pulsed dc method, as well as its characterization by XRD, XPS, and Raman spectroscopy [9]. Other studies of CrAlN coatings deposited by unbalanced magnetron sputtering and different Cr and Al concentrations from sectioned targets demonstrated a good corrosion resistance and adhesion to substrate when Cr and Al content was increased [20]. However, to our knowledge, there are no published studies of CrAl/CrAlN coatings deposited by HIPIMS on AISI-A11 tool steel of sectioned targets and their mechanical and tribological properties.

The aim of this research was to modify tribological and mechanical properties of an AISI-A11 tool steel by means of two CrAl/CrAlN multilayer architecture coatings and the effect of a solid lubricant top layer (a-CN<sub>x</sub>) deposited by HIPIMS for the wide applications in potential engineering fields.

## 2. Materials and Methods

### 2.1. Sample Preparation and Film Deposition

All the coatings were deposited by HIPIMS in a tempered (55 HRC), commercial A11 tool steel (AISI A11), and they were mechanically polished until a roughness of  $R_a = 40$  nm. The distance of the substrate to the target was 7 cm. Moreover, silicon substrates (99.999% purity, crystal orientation  $\langle 111 \rangle \pm 0.5^\circ$ ) were deposited in order to make thickness measurements; a schematic of the coating process is shown in Figure 1a. All the samples were degreased and cleaned in an ultrasonic bath with acetone and absolute alcohol and dried with  $N_2$ . CrAl/CrAlN multilayer coatings were deposited from a 50:50 vol.% CrAl target (two-inch diameter and 99.95% purity); target configuration can be seen in Figure 1b. Meanwhile, in the CrAl/CrAlN (a-CN<sub>x</sub>) multilayer, the a-CN<sub>x</sub> phase was deposited using a C target (2 inch in diameter and 99.95% purity); the target after the coating process is shown in Figure 1c. Argon and nitrogen (99.9999% purity) as working and reactive gases, respectively, were supplied into the chamber. The base pressure prior to deposition was  $3.99 \times 10^{-4}$  Pa. CrAl layers were deposited at 0.66 Pa with an Ar flow rate of 20 sccm, while a reactive N<sub>2</sub> flow rate of 13.5 sccm in a 1.48 Ar/N<sub>2</sub> ratio was used for both CrAlN and a-CN<sub>x</sub> layers. A HIPIMS pretreatment was performed with a CrAl target in Ar atmosphere for 12 min in order to enhance the adhesion. Deposition parameters and the deposition sequence of the CrAl/CrAlN and CrAl/CrAlN-(a-CN<sub>x</sub>) multilayer are summarized in Table 1.

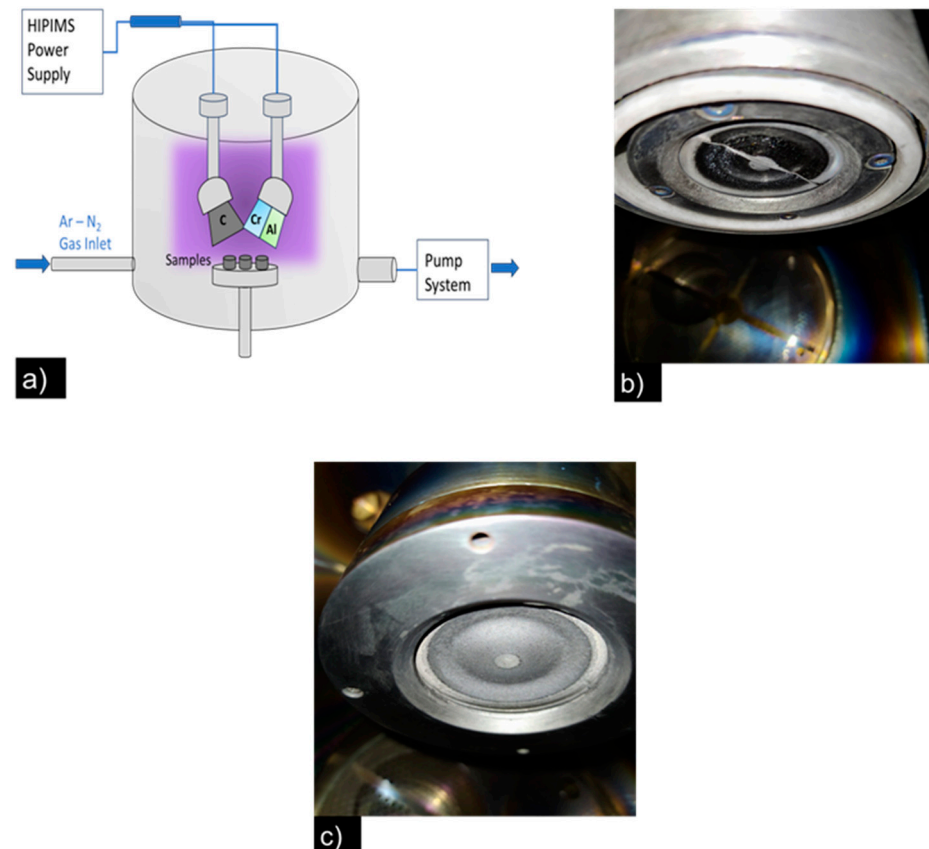


**Figure 1.** (a) Schematic of the high-power impulse magnetron sputtering system (HIPIMS). (b) Cr-Al target (0.50:0.50) area ratio after the coating process and (c) the C target after the coating process.

**Table 1.** Architecture and deposition parameters of multilayers.

Sample ID	Layer		Pulse Width ( $\mu$ s)	Frequency (Hz)	Voltage (V)	Peak Current (A)	Thickness/Period (nm)	Time (min)
	Periods	Composition						
S1	4	CrAl	20	300	610	34	155 $\pm$ 4.0	12
	4	CrAlN	20	300	420	50	235 $\pm$ 5.8	45
S2	3	CrAl	20	300	610	34	155 $\pm$ 4.0	12
	3	CrAlN	20	300	420	50	235 $\pm$ 5.8	45
	1 top layer	CNx	30	300	735	53	85 $\pm$ 3.1	13

## 2.2. Structure, Morphology, and Chemical Characterization

Cristal characterization coatings were conducted by X-ray diffraction spectra with a Cu-K $\alpha$  Cu radiation ( $\lambda = 0.15418$  nm) under an energy of 30 kV, 30 mA, with 0.01  $^\circ$ /s as the scan rate in a  $2\theta$  range of 30–90 $^\circ$  (by means of D8 Advance Bruker diffractometer). The (a-CNx) top layer, the wear tracks of multilayers, and the counter body were analyzed by Raman spectroscopy using a confocal microscope (DXR, Thermo Fisher Scientific, Waltham, MA, USA) with a 532 nm laser wavelength. The Gaussian function was used for peak deconvolution and fitting. Wear tracks of multilayers deposited on steel, as well as the thickness and morphology of the cross-section of the multilayer deposited on the silicon substrate were observed by field emission scanning electron microscopy (FESEM), Tescan, MIRA 3 LMU. Roughness measurements over surface substrates and multilayer coatings were made by means of a Stylus profilometer (Dektak 150), with a stylus type 2.5  $\mu$ m radius. Chemical composition of the multilayer was analyzed by X-ray fluorescence (XRF—S2 PUMA series 2 Bruker, Billerica, MA, USA).

## 2.3. Mechanical and Adhesion Properties

Nanoindentation tests were made according to ASTM E2546 standards and the Oliver Pharr method [21]. A normal load of 8 mN was used with a Berkovich diamond indenter, calibrated by nanoindentation testing over a wide load range on fused silica reference samples, and a total of nine indentations were realized in each sample. Measurements were performed to evaluate hardness and elastic modulus using a mechanical tester CB500 Nanovea. The indentation depth was less than 10% of the multilayer film thickness in order to avoid the effect of substrate on hardness measurements. The elastic recovery (ER) of multilayer films was calculated according to the following Equation (1):

$$\frac{(L_{max} - L_{res})}{L_{max}} \times 100\% \quad (1)$$

where  $L_{max}$  is the indentation depth at maximum load, and  $L_{res}$  is the residual depth after unloading. Root mean square roughness ( $R_a$ ) of the top layer film was measured by contact profilometry. All measurements were made with a scan length of 10 mm and a scan time of 240 s. Adhesion strength was measured by the nano scratch test according to ASTM C1624 standards with the following parameters: maximum load of 1300 mN, with a loading rate of 200 mN/min, and scratch length of 0.5 mm. The critical load ( $L_c$ ) of each multilayer film was plotted on the images obtained through the scanning electron microscope. The critical load ( $L_{c1}$ ) is where the crack initiates; meanwhile, the critical load ( $L_{c2}$ ) is where the coating delamination occurs. Adhesion energy of the interfacial crack, where the Griffith energy approach has been adopted by some researchers [22–24], is shown in Equation (2):

$$G_c = \frac{\sigma_c^2 t}{2E_f} \quad (2)$$

where  $t$  and  $E_f$  are the thickness and elastic modulus of coatings, respectively; and  $\sigma_c$  is the critical stress for coating delamination from the substrate, which is calculated from the following Equation (3) [25]:

$$\sigma_c = \left( \frac{2L_{c2}}{\pi d_c^2} \right) \left[ \frac{(4 + \nu_f)3\pi\mu}{8} - (1 - 2\nu_f) \right] \quad (3)$$

where  $L_{c2}$  is the critical load,  $d_c$  is the track width when delamination occurs,  $\mu$  is the friction coefficient, and  $\nu_f$  is the Poisson ratio for the coating according to some references [26–28].

#### 2.4. Tribological Properties

In order to evaluate tribological properties of multilayers with a tribometer tester (Triboscreen Ducom, Peenya, Bengaluru, Karnataka, India), a fretting test was carried out, varying normal load (40, 60, and 80 N). A set of three tests for load was performed with a stroke length of 150  $\mu\text{m}$ , frequency of 2 Hz, 10,000 cycles at room temperature (23  $^\circ\text{C}$ ), and relative humidity from 48 to 53%. Characteristic curves to investigate fretting wear damages is the plotting of the called fretting loop, which is related to the evolution of the tangential force versus displacement. Friction force between the contact pairs ( $F_f$ ), displacement amplitude ( $\delta$ ), normal load ( $F_n$ ), and friction energy ( $E_d$ ), which correspond to the area of the fretting loop, were obtained from this plot [29]. Each parameter for a complete fretting loop [30] was related to the friction force and displacement amplitude. Meanwhile, each fretting loop corresponded to a fretting wear regime for partial slip and gross-slip.

### 3. Results and Discussion

#### 3.1. Structure, Morphology, and Chemical Characterization

The crystalline structures of multilayer CrAl/CrAlN (sample labeled as  $S1$ ) and CrAl/CrAlN-a-CN<sub>x</sub> (sample labeled as  $S2$ ) were cubic, as can be seen in Figure 2a. All the diffraction peaks from the planes (111), (200), (220), and (222) of the coated samples could be indexed similar to the CrN structure, and it is well known that the standard CrN (200) peak is at 43.59 $^\circ$  (JSPDF 65-2899) [4,31,32]. However, the CrAlN (200) peaks (JCPDS 25-1495) in samples  $S1$  and  $S2$  were around 43.69 $^\circ$  and 43.89 $^\circ$ , respectively (see Figure 2a). This deviation observed in the main peaks (200) could be attributed to a decrease in the lattice parameter from the CrN phase (4.149  $\text{\AA}$ ) compared to the CrAlN phase (4.14 and 4.122  $\text{\AA}$  in samples  $S1$  and  $S2$ , respectively). This is attributed to the Al atoms into the CrN phase, and these results agree well with those reported previously [9,15,33–36].

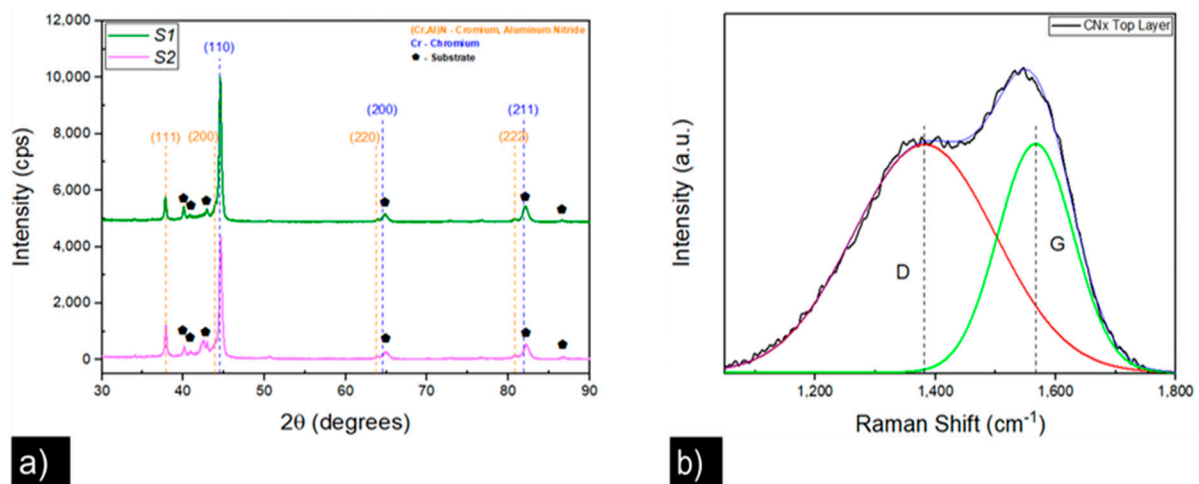
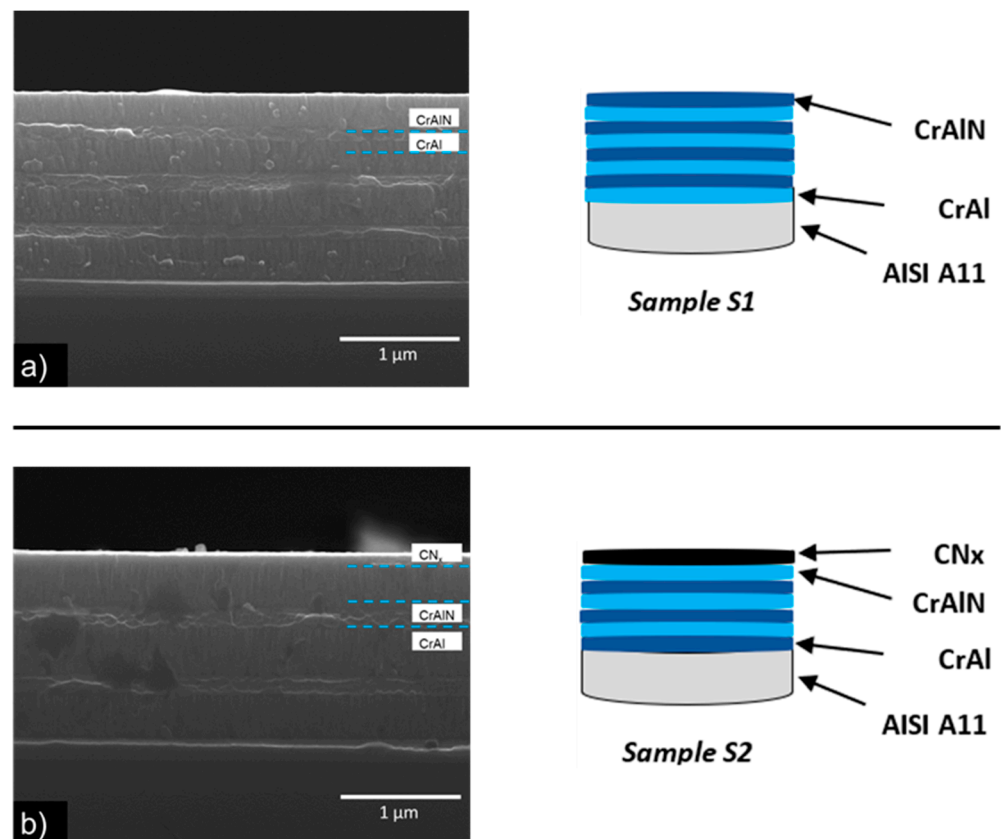


Figure 2. XRD diffractograms: (a) for sample  $S1$  and  $S2$ . Raman spectrum: (b) CN<sub>x</sub> top layer.

In the other hand, sample *S2* with an (a-CN<sub>x</sub>) top layer was characterized by Raman spectroscopy. The Raman spectra shown in Figure 2b present the characteristic peaks of disorder (D) and graphitic (G) due molecular vibrations in the (a-CN<sub>x</sub>) thin film. The peak centered at 1375 cm<sup>-1</sup> was associated with a disordered band (D); meanwhile, the graphitic band (G) was located at 1562 cm<sup>-1</sup>. These results have been observed for pure carbon films, where peaks are located between 1200 and 1700 cm<sup>-1</sup>, and peaks are associated with sp<sup>2</sup> C sites [18,37]. Some studies on amorphous carbon nitride coatings showed that the G band appeared by the C-C stretching vibrations of sp<sup>2</sup> bonds, and meanwhile the D band was associated with breathing modes in both sp<sup>2</sup> rings and chains [38,39].

Multilayer coating thickness and morphology were determined by means of fracture cross-section of silicon substrates using secondary electron SEM images, as can be seen in Figure 3a,b for samples *S1* and *S2*, respectively. Multilayer thickness for sample *S1* was 1.5 μm, while sample *S2* presented a total thickness of 1.2 μm. The CrAl phase showed a glassy morphology in both samples, with a (a-CN<sub>x</sub>) top layer in the *S2* sample (see Figure 3b). Similar results have been reported in other studies [9,17,40,41]. However, the CrAlN phase presented the characteristic columnar morphology in both samples *S1* and *S2*, as can be see in Figure 3a,b, respectively. Similar results were observed in CrAlN coatings deposited by HIPIMS [3,12]. For the root mean square roughness (R<sub>a</sub>) measurement made of the top multilayer coatings, a total of 12 measurements were made to each sample. Results show a R<sub>a</sub> = 0.03628 μm ± 0.0058 for sample *S1*, while for sample *S2*, the R<sub>a</sub> = 0.02636 μm ± 0.0055; these changes in = roughness can be attributed to the (a-CN<sub>x</sub>) top layer, and the results agree well with others reported previously [35,42].



**Figure 3.** SEM cross-section micrographics: (a) sample *S1* and (b) sample *S2*.

The chemical compositions of the bulk multilayer coatings are listed in Table 2. XRF results showed a light discrepancy for the Cr and Al concentrations between samples *S1* and *S2*. This difference can be attributed to the different sputtering yields between the Cr and Al

species when reactive atmosphere is deposited [9,43] and there are equipment limitations to quantifying light elements by XRF analysis.

**Table 2.** XRF atomic composition of multilayer samples *S1* and *S2*.

Sample ID:	Atomic Composition (at.%)		
	Cr	Al	N
<i>S1</i>	32.46	66.30	-
<i>S2</i>	27.52	69.74	-

### 3.2. Mechanical and Adhesion Properties

Results from the nanoindentation test showed hardness values of  $23.08 \pm 2.8$  GPa and  $20.58 \pm 1.8$  GPa for samples *S1* and *S2*, respectively (see Figure 4a,b). The elastic modulus values were  $508 \pm 39.3$  GPa and  $397 \pm 33.6$  GPa for samples *S1* and *S2*, respectively. Similar results (520 GPa) were reported for CrAlN coatings obtained with two targets of Cr and Al [7]. Table 3 shows the summarized values for mechanical properties. Similar hardness values were observed in other studies over monolayer CrAlN and multilayer CrAlN/CN<sub>x</sub> films obtained for HIPIMS and ion-beam-assisted magnetron sputtering [3,7,12,15]. As can be seen in some studies, hardness values, Young's modulus, and toughness are related to the multilayer microstructure, as well as residual stress, which can increase the hardness due to the dislocation motion blocking. It has been seen that the CrAl layer increases the hardness of the CrAlN phase, which presents high elastic modulus [40]. So, alternating the layers of both phases improves the mechanical properties, and the increase in hardness can be explained by the Hall–Petch effect [44]. On the other hand, sample *S2* shows a reduction in hardness values (10%), and the elastic modulus values of 22% can be compared to sample *S1*.

**Table 3.** Mechanical properties of CrAl/CrAlN and CrAl/CrAlN/CN<sub>x</sub> multilayers.

Sample ID:	Thickness (μm)	<i>Ra</i> (μm)	<i>H</i> (GPa)	<i>E</i> (GPa)	<i>E<sub>r</sub></i>	<i>H/E</i>	<i>H<sup>3</sup>/E<sup>2</sup></i>	<i>H/E<sub>r</sub></i>	<i>ER</i> (%)
<i>S1</i>	1.5 ± 0.06	0.03628 ± 0.0058	23.08 ± 2.8	508 ± 39.3	373	0.045	0.047	0.0617	36.24
<i>S2</i>	1.2 ± 0.05	0.02636 ± 0.0055	20.58 ± 1.8	397 ± 33.6	305	0.051	0.055	0.0674	45.75

From the typical loading–unloading curve for these samples, the area between the loading and the unloading curve represents the energy dissipated into the film by the plastic deformation designated as  $D_p$ , while the area under the unloading curve represents the elastic energy deformation represented by  $D_e$ . The *S1* sample had a mayor  $D_p$  area compared to the *S2* sample, which could be attributed to its superior hardness ( $23.08 \pm 2.8$  GPa) compared to sample *S2* ( $20.58 \pm 1.8$  GPa), where the (a-CN<sub>x</sub>) top layer and carbon morphology increased absorption energy capacity. The difference in hardness agreed well with the minor  $D_e$  area in sample *S1* and the less mechanical potential energy stored can be attributed to the more ceramic content in its multilayer architecture. These results agreed well with the elastic recovery values (*ER*) obtained from Equation (1). Sample *S1* showed a value of 36.24%, while sample *S2* had a higher value of 45.75%. Moreover, the reduction in hardness and elastic modulus from the whole multilayer can be attributed to the (a-CN<sub>x</sub>) top layer morphology, in which similar values have been reported [40]. Mechanical resilience of multilayer films was extracted from  $H/E_r$  relation, regarding the elastic and plastic behavior for these materials. According to obtained results, sample *S2* presented a higher value of 0.0674 compared to the value of 0.0617 obtained in sample *S1*. This small increase in sample *S2* can be attributed to the (a-CN<sub>x</sub>) top layer and its resilient capacity [18], and these results agree well with some studies that report low elastic modulus values and are associated to low coefficient friction [45], as was the case in sample *S2*.

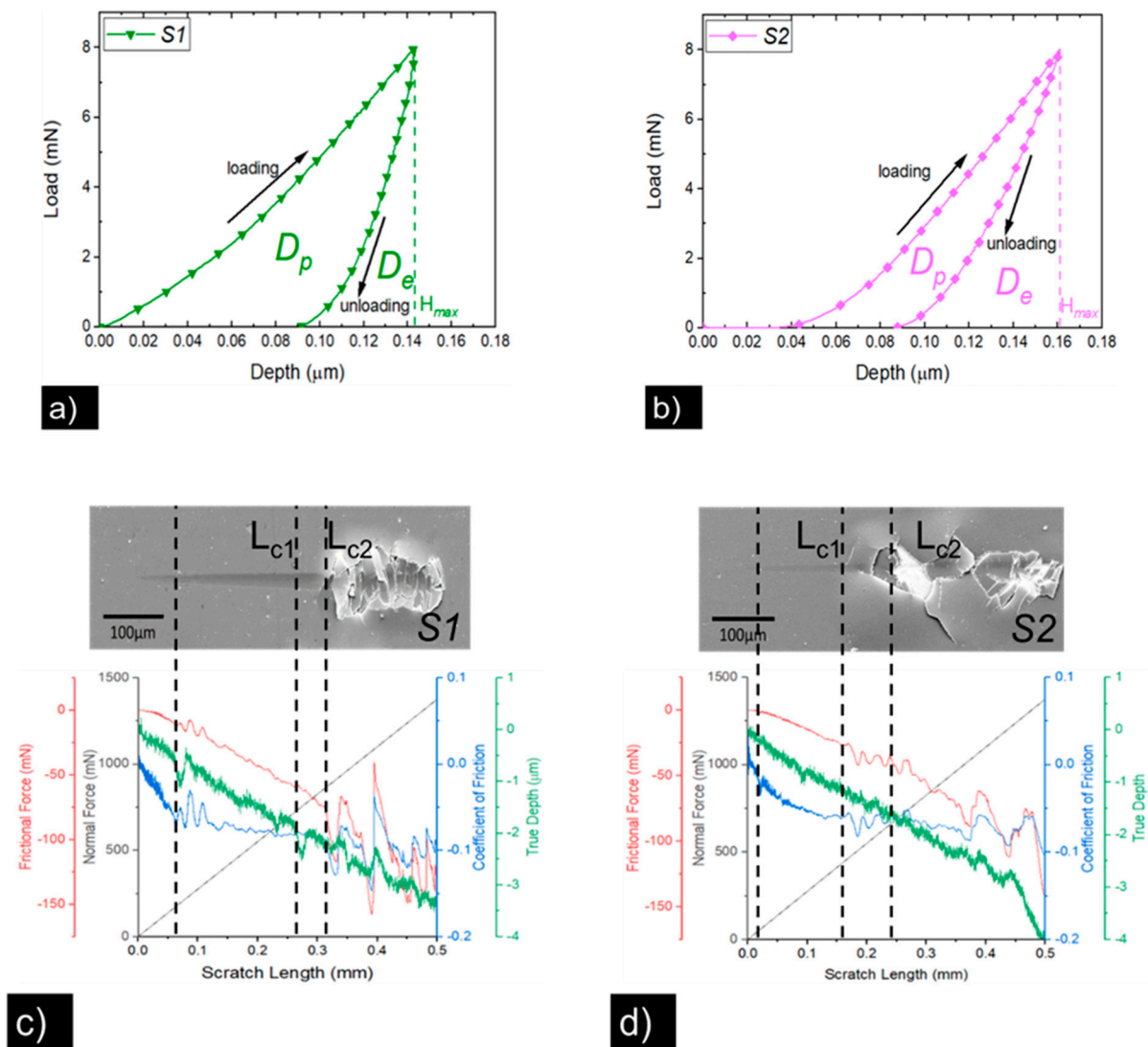


**Figure 4.** Load-displacement graphic test: (a) *S1* sample and (b) *S2* sample. Progressive load scratch test data and SEM image: (c) *S1* sample and (d) *S2* sample.

Figure 4c,d shows the nano scratch test results for samples *S1* and *S2*, respectively. Critical loads of crack initiation length ( $L_{c1}$ ) and delamination length ( $L_{c2}$ ) were extracted from electronic images and are indicated by dotted lines in the plotted graphics. Results are summarized in Table 4. The  $L_{c1}$  varied from 0.729 N to 0.434 N for samples *S1* and *S2*, respectively. According to these values, sample *S1* presented the strongest scratch resistance, and in the same way, sample *S1* showed the highest  $L_{c2}$  value of 0.859 N while sample *S2* presented a  $L_{c2}$  value of 0.665 N. This difference could be attributed to the higher thickness and elastic modulus in sample *S1* compared to *S2*.

**Table 4.** Friction coefficient, critical load, critical stress, and adhesion energy obtained by nano scratch tests.

Sample ID:	$\nu$	$\mu$	$L_{c1}$ (N)	$L_{c2}$ (N)	$\sigma_c$ (GPa)	$G_c$ (J/m <sup>2</sup> )
<i>S1</i>	0.22	0.086	0.729	0.859	0.5339	0.5329
<i>S2</i>	0.19	0.056	0.434	0.665	0.3755	0.2539

Using Equations (2) and (3), adhesion energy and the critical stress for each coating are listed in Table 4. Here, the sample *S1* showed the highest adhesion energy of 0.532 J/m<sup>2</sup>,

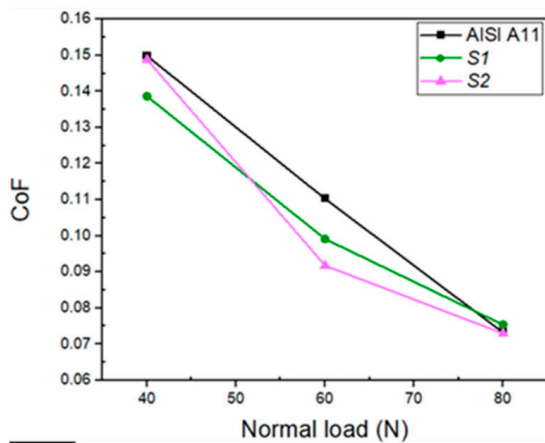
while sample S2 showed only  $0.253 \text{ J/m}^2$ . Adhesion strength in sample S1 corresponded to the largest coefficient of friction ( $0.086 > 0.056 \mu_k$ ), and similar results have been reported by several authors [46,47]. On the other hand, sample S1 presented higher roughness values than sample S2. Higher roughness could act like obstacles to movement of the indenter due to the high ridges and valleys, which increase the critical load ( $L_{c2}$ ) [47,48]. These different roughness levels could increase the density of defects in the coating and at the interface, affecting the adhesion strength. Other studies reported that the adhesion to the substrate of the multilayer films decreased as the (a-CN<sub>x</sub>) sublayer thickness increased [49]. These results agree well with lower adhesion resistance observed in sample S2. Here, this lower adhesion resistance can be attributed to the residual stress generated in the CN<sub>x</sub> top layer, as has been reported in other studies [18,49].

### 3.3. Tribology Properties

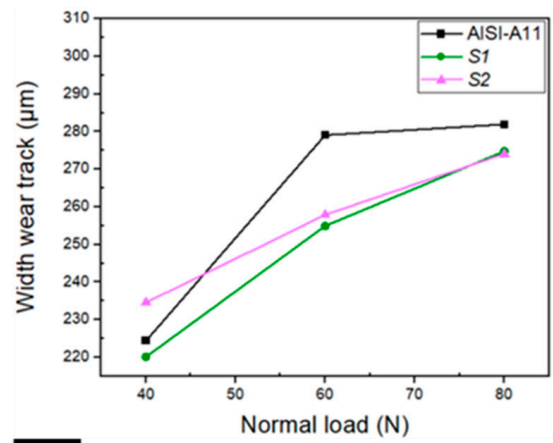
Figure 5a shows the plot corresponding to average CoF vs. applied load for samples S1 and S2, respectively. For an applied load of the 40 N sample, S1 showed a lower CoF value ( $0.13865 \pm 0.00389 \mu_k$ ) compared to the S2 sample ( $0.14884 \pm 0.00472 \mu_k$ ). When the applied load increased to 60 N, sample S2 showed an abrupt change in the CoF value ( $0.09175 \pm 0.00336 \mu_k$ ) compared to sample S1 ( $0.09915 \pm 0.0030 \mu_k$ ). Meanwhile, CoF values for sample S2 ( $0.07296 \pm 0.00228 \mu_k$ ) and S1 ( $0.07537 \pm 0.0025 \mu_k$ ) were close when a load of 80 N was applied. The width wear track for the fretting wear test is shown in Figure 5b, wherein sample S2 showed a higher value for width wear track ( $234.58 \pm 6.7 \mu\text{m}$ ) compared to sample S1 ( $220.13 \pm 7.9 \mu\text{m}$ ) tested with a normal load of 40 N. When a normal load of 60 N was applied, the difference in the width wear track ( $257.88 \pm 8.4 \mu\text{m}$ ) in sample S2 compared to sample S1 ( $254.91 \pm 5.5 \mu\text{m}$ ) was lower. Finally, sample S1 showed a higher value of ( $274.77 \pm 3.9 \mu\text{m}$ ) compared to the value for sample S2 ( $274.07 \pm 3.4 \mu\text{m}$ ) as soon as the normal load was increased to 80 N. As was observed, the coefficient of friction in fretting conditions decreased as normal load was increased (Figure 5a).

Otherwise, after low normal loads were applied, there was an elastic contact between the surface of the thin film and ball of alumina, hence the slip spread over the contact area. The debris detached during the wear process was trapped between the contact zone, increasing the coefficient of friction at low normal loads. Conversely, at high normal loads, the surface was under an elastic–plastic state, resulting in a low coefficient of friction, and as the wear track was in function of normal load, as it increased, the wear track increased. Similar results were observed in previous studies [50–52]. The wear volume as a function of normal loads is shown in Figure 5c, with lower values for sample S1 ( $1.84 \times 10^5$  and  $3.32 \times 10^5 \mu\text{m}^3$ , respectively) at normal loads of 40 and 60 N compared to sample S2 ( $2.38 \times 10^5$  and  $3.47 \times 10^5 \mu\text{m}^3$ , respectively). Similar values of wear volume ( $4.48 \times 10^5$  and  $4.43 \times 10^5 \mu\text{m}^3$ ) were observed for samples S1 and S2, respectively, when a normal load of 80 N was applied. Figure 5d–f shows the CoF behavior for samples S1 and S2 vs. different cycles and a comparison for when normal load was increased. As can be seen, stable CoF behavior was observed for both samples during different cycles in the fretting wear test.

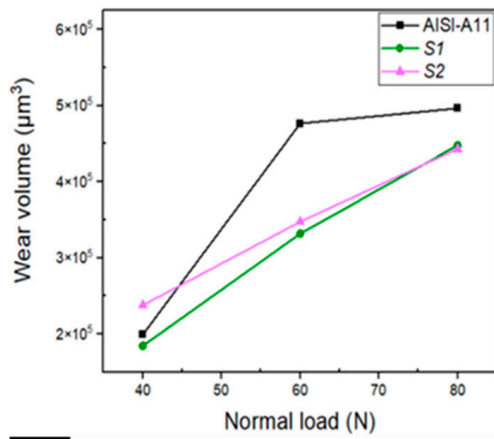
Figure 6a,b shows the FESEM wear track for sample S1, and we magnified the analyzed zone for the fretting wear test at 40 N. As can be seen, the wear track had an elliptical shape and showed a principal damage in the center of the track, with the main wear mechanism being delamination followed by partial ploughing and cracking. As can be seen in Figure 6c,d, an increment in the normal load to 60 N resulted in a concentric wear track with apparently less surface damage, mainly composed of ploughing and delamination. Finally, as shown in Figure 6e,f, when the normal load was 80 N, the wear track showed a displacement until it was stabilized. At the center of the wear track, no damage was seemingly observed, with only a crater wear mechanism. From the wear tracks (see Figure 6a–f) for different normal loads applied during the fretting test, it was evident that there was a change in the damage, width wear track, and wear mechanism, which agreed well with the change in CoF values reported above (see Figure 5a).



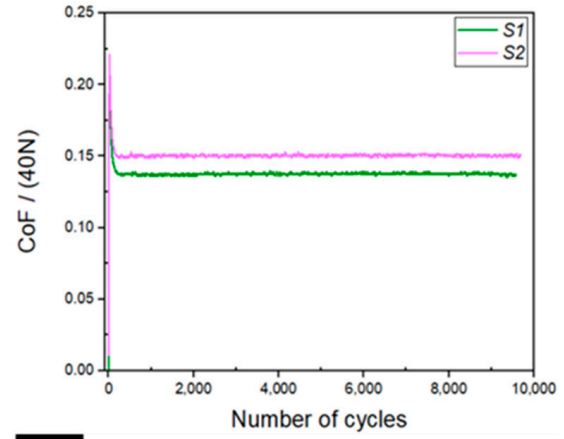
a)



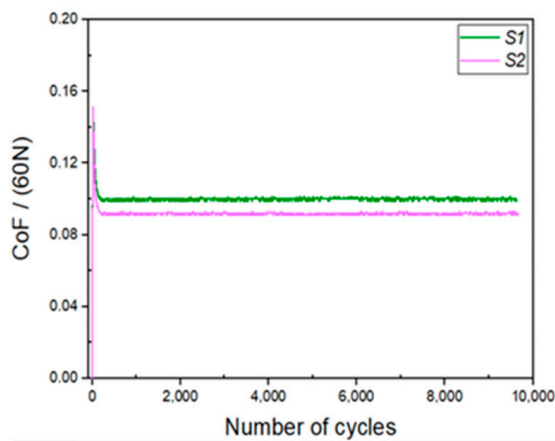
b)



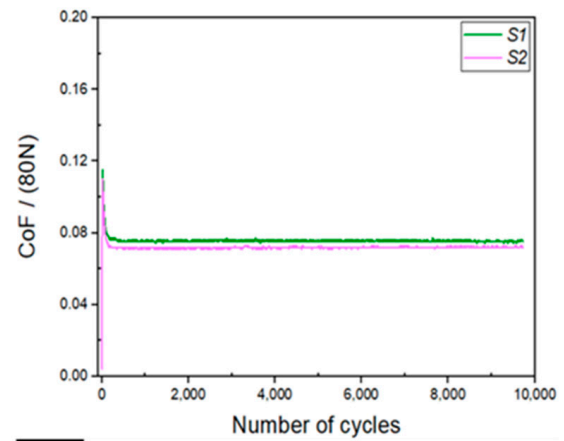
c)



d)



e)



f)

**Figure 5.** (a) Coefficient of friction as a function of different normal loads for samples *S1* and *S2*. (b) Width wear track as a function of different normal loads. (c) Wear volume as function of normal loads. (d) Variation of coefficient of friction at a 40 N normal load. (e) Variation of coefficient of friction at a 60 N normal load. (f) Variation of coefficient of friction at a 80 N normal load.

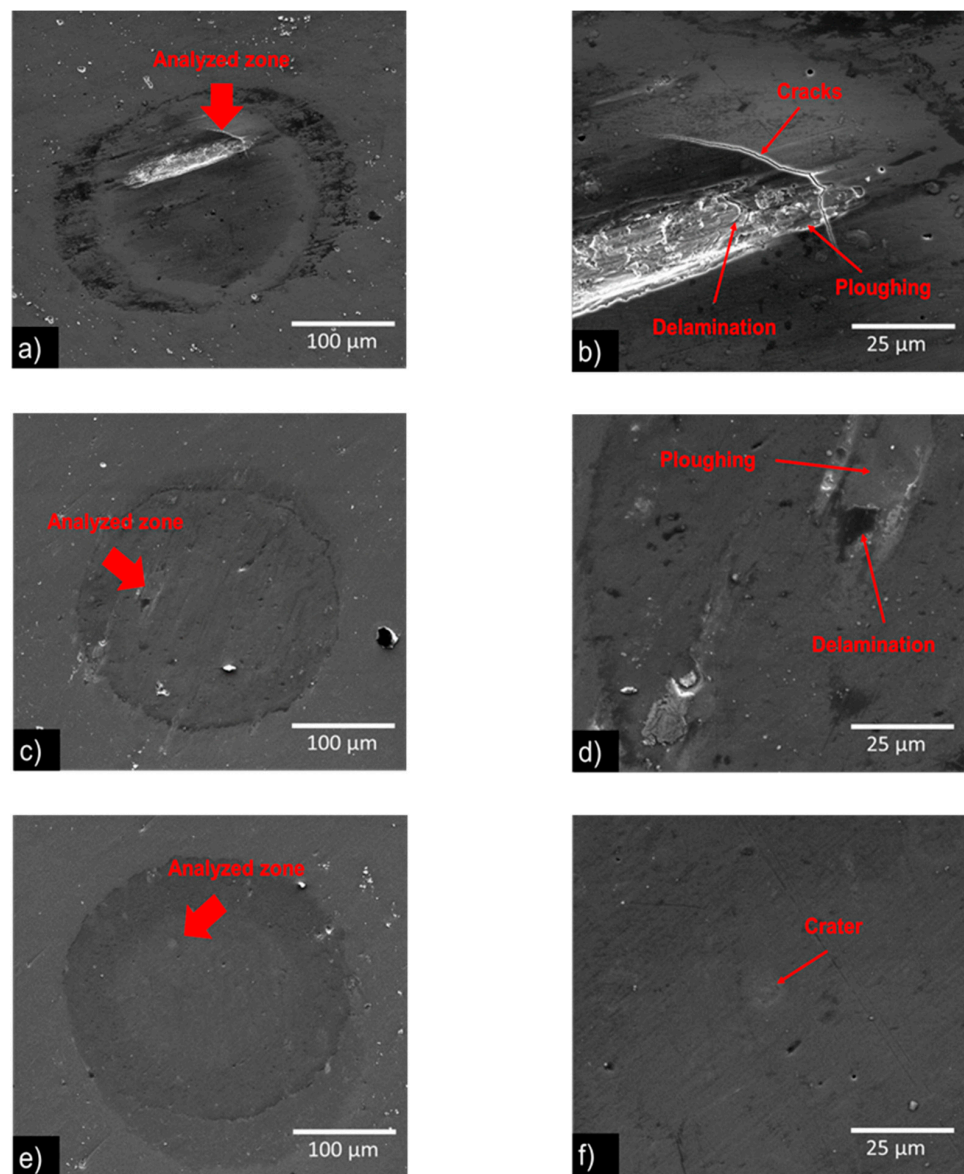


**Figure 6.** Wear tracks from sample *S1* under the fretting test with different loads: (a) 40 N, (b) ampliation, (c) 60 N, (d) ampliation, (e) 80 N, and (f) ampliation.

The FESEM images of wear track of sample *S2* are shown in Figure 7. Under a normal load of 40 N, a concentric wear track is appreciated, and the main wear mechanism is crater formation followed by cracks, as can be seen in Figure 7a,b. When the load increased to 60 N, a similar shape wear track was observed, with a ploughing wear mechanism, as can be seen in Figure 7c,d. As the load increased to 80 N, the wear track was observed due to the ball displacement, and it diminished once the tests stabilized; however, no damage was seemingly observed, only a crater wear mechanism, as can be seen in Figure 7d,e. Compared to sample *S1*, the wear tracks for sample *S2* showed less damage and regular shape during the fretting test, besides the lowest CoF values; however, this sample presented a larger width wear track that could be attributed to the slip spread contact area over the top (a-CN<sub>x</sub>) layer (see Figure 3b), which worked as a solid lubricant, decreasing the friction force between the surface in contact during the fretting wear test. It has been reported for micro tribological tests on (a-CN<sub>x</sub>) films that after cycles running the test, it contributes to the formation of a graphitic-like transfer film named a tribolayer, which helps to maintain the CoF value in a steady state; during the wear test, the same results were reported over (a-CN<sub>x</sub>) layer deposited by HIPIMS [53].

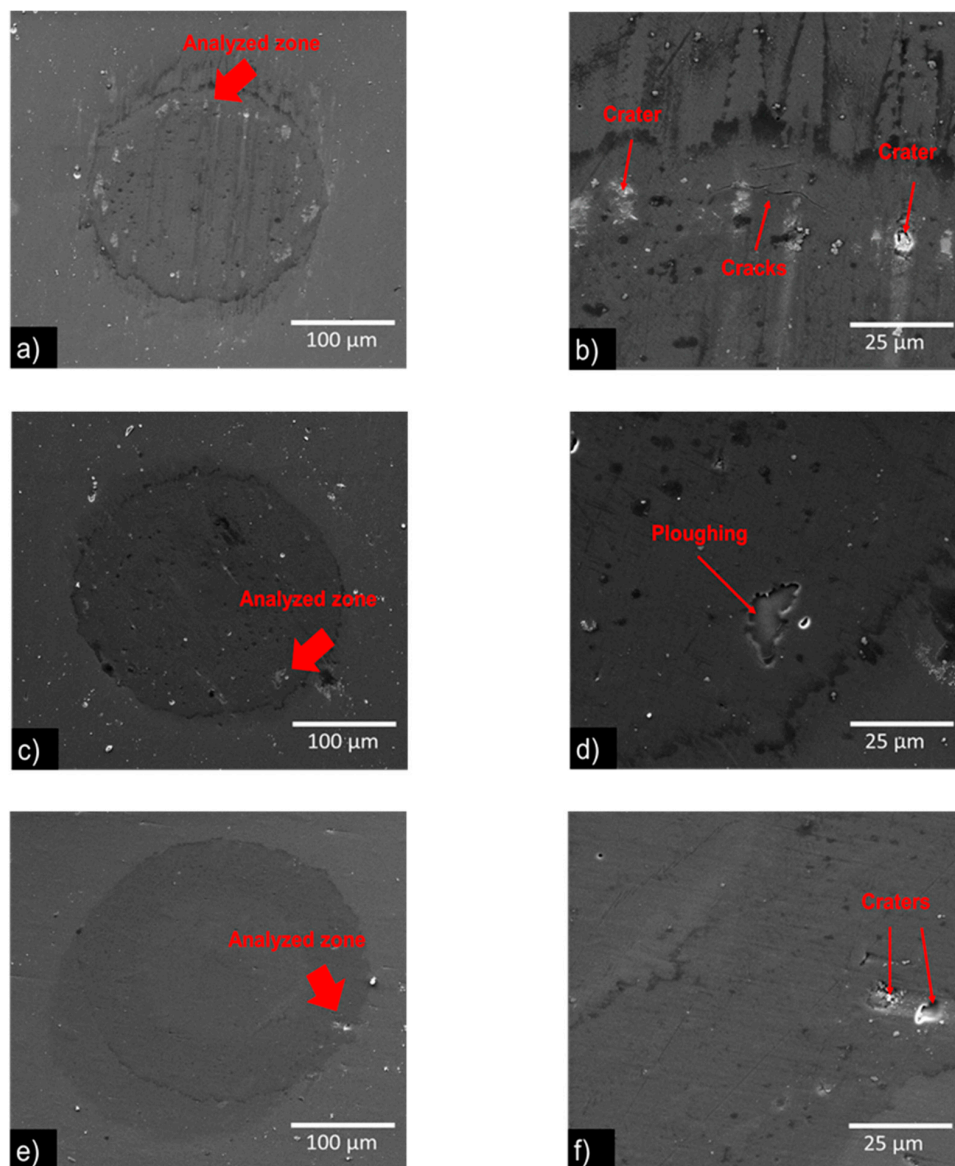


**Figure 7.** Wear tracks from sample *S2* under fretting test with different loads: (a) 40 N, (b) ampliation, (c) 60 N, (d) ampliation, (e) 80 N, and (f) ampliation.

A way in which to see the aptness of tribology is through the relation  $(H/E)$  and resistance to plastic indentation  $(H^3/E^2)$  ratio based on nanoindentation results. As can be seen in Table 3, sample *S2* showed higher values for  $H/E$ : 0.051 and  $H^3/E^2$ : 0.055, compared to sample *S1*, even for less multilayer thicknesses of 1.2  $\mu\text{m}$  and 1.5  $\mu\text{m}$ , respectively. These results agree well with other studies for CrAlN and (a-CN<sub>x</sub>) layers [2,3,7,42]. However, tribological properties in multilayer coatings depend on multiple factors such as microstructure, grain size, density, and residual stress.

### 3.3.1. Raman Characterization in Fretting Test

Figure 8a–f shows the Raman spectra analysis performed on the wear track surface for the sample *S1* and the Al<sub>2</sub>O<sub>3</sub> ball counter face after the fretting wear test. Figure 8a shows bands at higher numbers around 1400  $\text{cm}^{-1}$  and 2400  $\text{cm}^{-1}$ , while as seen in Figure 8b, the Al<sub>2</sub>O<sub>3</sub> counter face showed weak intense peaks around 400  $\text{cm}^{-1}$ , and others at 2400  $\text{cm}^{-1}$ . At a higher load of 60 N, the Raman spectra showed peaks for the wear track at 650 and 2400  $\text{cm}^{-1}$ , as can be seen in Figure 8c. The same peaks (400 and 2400  $\text{cm}^{-1}$ ) were observed in the Al<sub>2</sub>O<sub>3</sub> counter face, as is observed in Figure 8d. Finally, as seen in Figure 8e, Raman

spectra corresponding to a normal load of 80 N was applied, showing peaks at 650 and 2400  $\text{cm}^{-1}$ , and Figure 8f shows the main peak at 2400  $\text{cm}^{-1}$  for the  $\text{Al}_2\text{O}_3$  counter face Raman spectra. Peaks values at 650  $\text{cm}^{-1}$  at the wear track corresponding to CrAlN Raman spectra were associated with longitudinal and transversal optical vibrations (LO and TO) at 400–650  $\text{cm}^{-1}$  [9]. Peaks at higher values arose via second-order transitions (A + O, 2O).

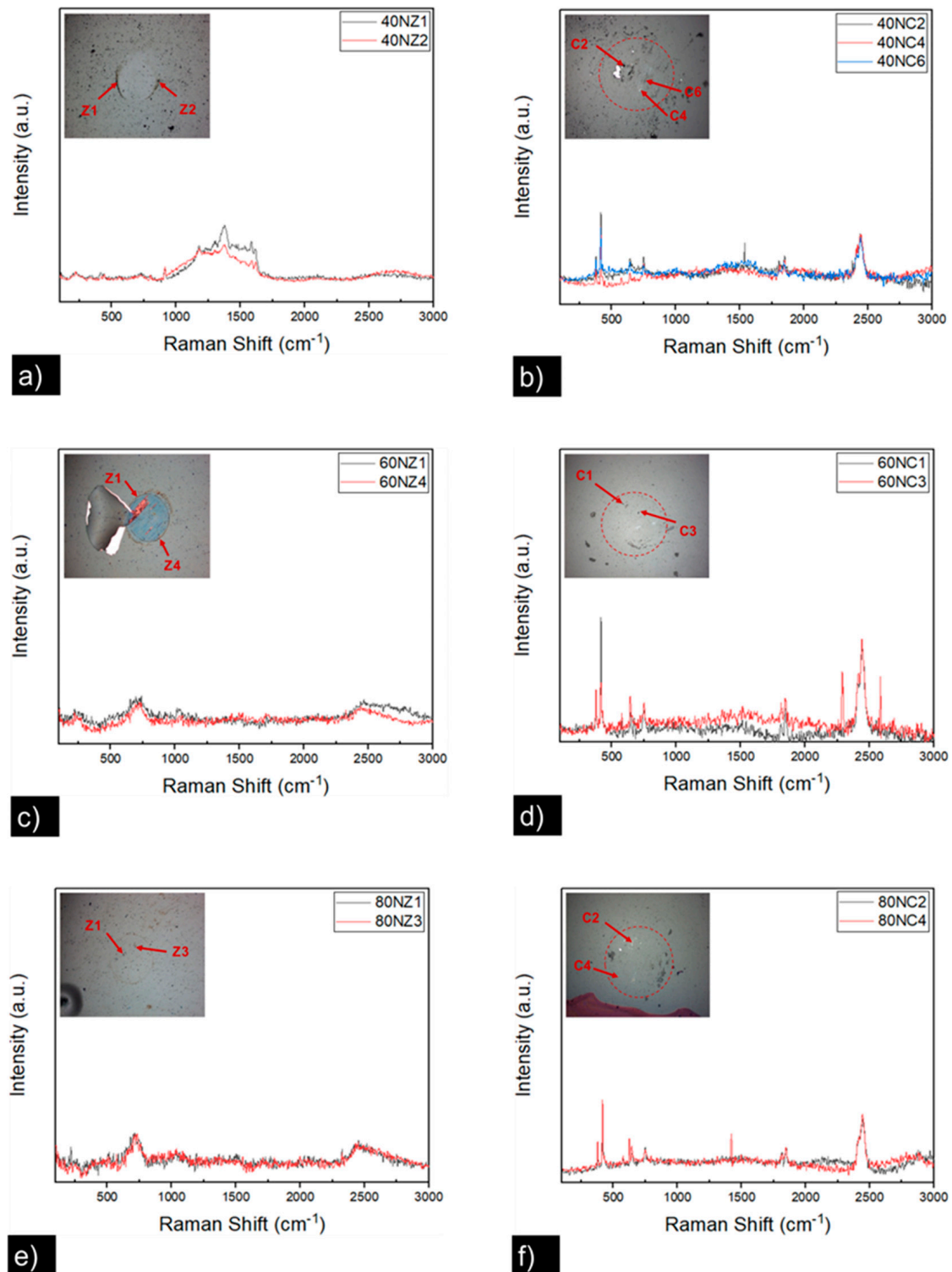


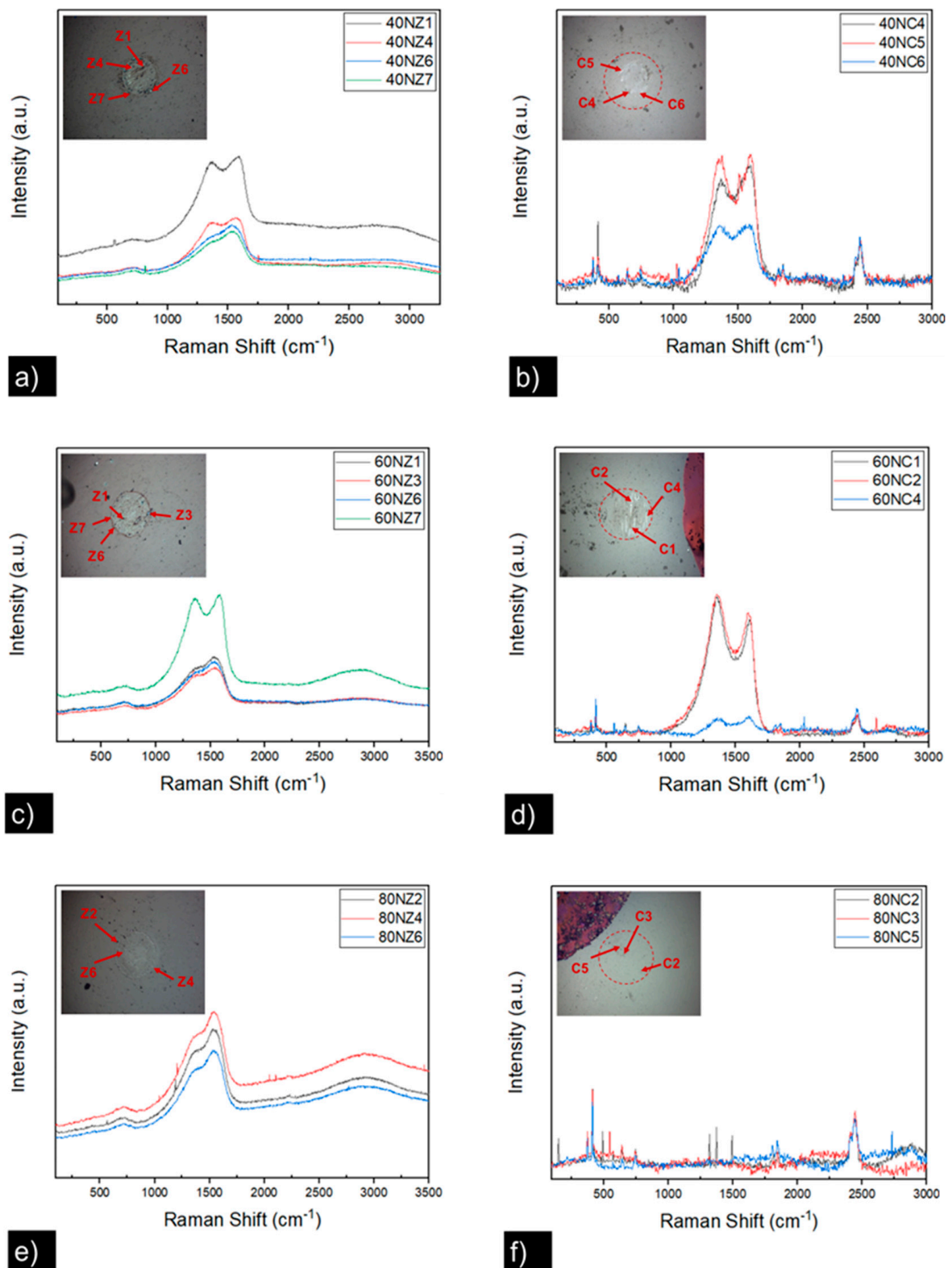
**Figure 8.** Raman analysis after the fretting wear test in sample S1: (a) wear track in the test at 40 N, (b) counter face track, (c) wear track in the test at 60 N, (d) counter face track, (e) wear track in the test at 80 N, (f) counter face track.

Meanwhile, higher peaks values of  $2400\text{ cm}^{-1}$  at the counter face corresponded to the  $\text{Al}_2\text{O}_3$  ball Raman spectra [54]; however, the weak peak of  $400\text{ cm}^{-1}$  could be a CrAlN film added to the surface. The same case was observed in the  $\text{Al}_2\text{O}_3$  counter face with a peak at  $400\text{ cm}^{-1}$  that could be attributed to the CrAlN film added to the  $\text{Al}_2\text{O}_3$  surface.

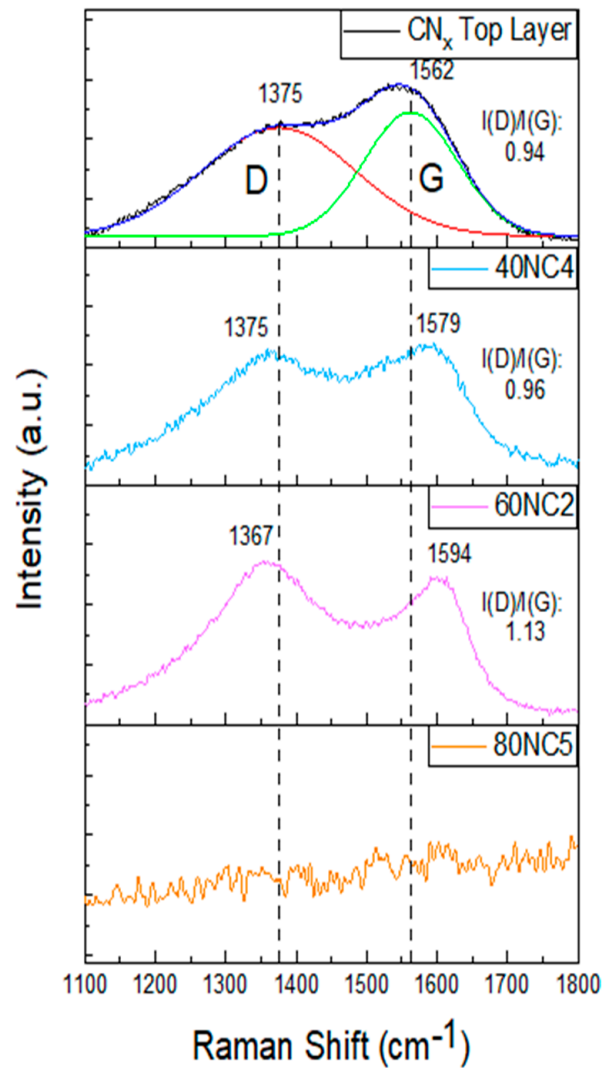
Raman spectra for sample S2 and the  $\text{Al}_2\text{O}_3$  ball counter face are shown in Figure 9. When a normal load of 40 N was applied, as shown in Figure 9a, there were high-intensity peaks between  $1350$  and  $1550\text{ cm}^{-1}$ . Meanwhile, Figure 9b shows peaks for the  $\text{Al}_2\text{O}_3$  counter face, with the same intensity peaks for  $1350$  to  $1550\text{ cm}^{-1}$ , followed by a peak at  $2400\text{ cm}^{-1}$ . When the normal load was increased to 60 N, as shown in Figure 9c, there were the same peaks between  $1350$  and  $1550\text{ cm}^{-1}$  and a less intense peak at  $2800\text{ cm}^{-1}$  in the wear track. As shown in Figure 9d, the  $\text{Al}_2\text{O}_3$  counter face showed an intense peak between  $1350$  and  $1550\text{ cm}^{-1}$  and a weak one at  $2400\text{ cm}^{-1}$ . An increment of 80 N in the normal load showed Raman spectra for the wear track seen in Figure 9e, with peaks between  $1350$  and  $1550\text{ cm}^{-1}$  and at  $2800\text{ cm}^{-1}$ . Lastly, the  $\text{Al}_2\text{O}_3$  counter face showed only a peak at  $2400\text{ cm}^{-1}$ , as was observed in Figure 9f, with no residue transfer of  $\text{CN}_x$  observed. This could be attributed to the  $\text{CN}_x$  top layer turned into small traces that were not adhered to the  $\text{Al}_2\text{O}_3$  counter face. Otherwise, Raman intensity peaks between  $1350$  and  $1550\text{ cm}^{-1}$  are characteristics of thin films for a- $\text{CN}_x$  [18] (see Figure 2b), and those at  $2800\text{ cm}^{-1}$  correspond with the  $\text{Al}_2\text{O}_3$  ball of Raman spectra [54]. The characteristic peaks for (a- $\text{CN}_x$ ) detected in the  $\text{Al}_2\text{O}_3$  counter face can be attributed to the tribo-layer formed during the fretting tests, which agrees with the wear volume removed during the test at 40 and 60 N normal loads, as can be seen in Figure 5c.

Figure 10 shows the typical Raman spectra subtracted from worn surfaces for sample S2 (see Figure 9) tested at 40, 60, and 80 N, compared to the deposited top layer (a- $\text{CN}_x$ ) with the deconvoluted peaks D and G. As can be seen, Raman spectra obtained of the worn surface tested at 40 N showed similar intensity for peaks D and G. The profile fitting results indicate that the value of  $I(\text{D})/I(\text{G})$  increased from 0.94 to 0.96.

On the other hand, Raman spectra of the worn surface obtained at 60 N showed a noticeable change in the intensity peaks D and G, compared to the as-deposited (a- $\text{CN}_x$ ) top layer, with a  $I(\text{D})/I(\text{G})$  ratio of 1.13. The increment of the  $I(\text{D})/I(\text{G})$  ratio can be attributed to the formation of the carbon  $\text{sp}^2$  structure (i.e., graphite-like structure), with previous studies having reported the same results [55], wherein this carbon structure is beneficial to low-friction coefficients ( $<0.10$ ) for carbon-based coatings [18,37,56]. Finally, no Raman spectra were observed in the  $\text{Al}_2\text{O}_3$  ball worn surface during the fretting test at 80 N, as can be seen in Figure 9f. This absence of transfer material from the  $\text{CN}_x$  layer can be attributed to the wear contact during the fretting test (see Figure 7e) and its fretting regime, which is detailed in the next section.



**Figure 9.** Raman analysis after the fretting wear test in sample S2: (a) wear track in the test at 40 N, (b) counter face track, (c) wear track in the test at 60 N, (d) counter face track, (e) wear track in the test at 80 N, (f) counter face track.



**Figure 10.** Deconvolution of Raman spectra of the  $\text{CN}_x$  top layer film deposited for sample S2 and worn surface during the fretting test at normal loads of 40 N (40NC4) and 60 N (60NC2).

### 3.3.2. Fretting Regime

The fretting maps and fretting loops are used to characterize the contact conditions at the contact interface [57,58]. Figure 11a,b defines each parameter for a complete fretting loop [30], which are related with the friction force and displacement amplitude. Meanwhile, Figure 11b,c shows a schematic of the fretting wear regime of contact, which are partial slip and gross-slip, respectively. Moreover, the area of the fretting loop can be calculated to determine the dissipated energy due to friction (which corresponds to wear volume according to the dissipated energy wear model) [59,60].

Figure 12a displays the fretting loop for sample S1 tested at 40 N of normal load for different cycles (2000, 4000, 6000, and 8000). As can be seen, the fretting loop shape corresponded to a partial slip regime. This agrees well with the contact wear track observed in Figure 6a. Figure 12b shows a fretting loop shape for a normal load of 60 N, which is in accordance with a gross slip regime that agrees well with the wear track observed in Figure 6c. It is evident that there was a variation displacement during the fretting test against different cycles. Finally, Figure 12c presents the fretting loop for a higher normal load of 80 N, wherein the regime changed again to a partial slip, and its respective wear track corresponded to this regime (see Figure 6e) [52].

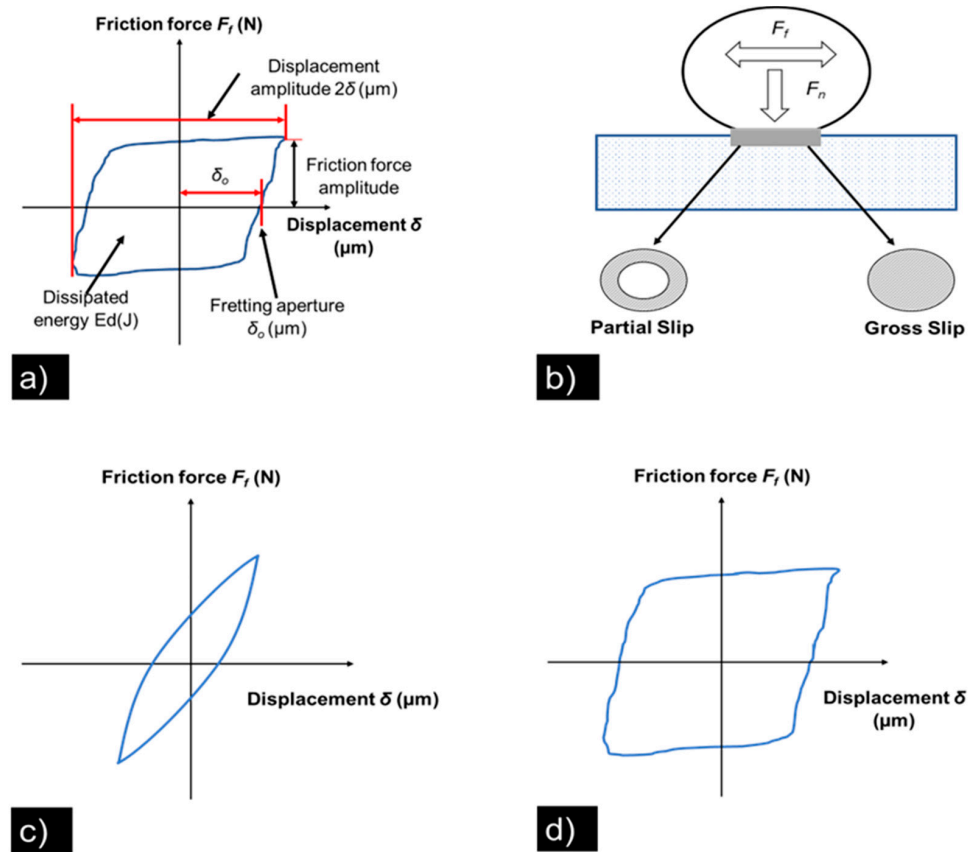


**Figure 11.** (a) Schematic of a fretting loop. (b) Illustration of fretting conditions. Fretting loop shape: (c) partial slip regime and (d) gross slip regime.

Figure 13 exhibits the fretting loops corresponding to sample S2. As can be seen in Figure 13a, there was a gross slip regime when a normal load of 40 N was applied, and the wear track agreed well with this result (see Figure 7a). A few variations of displacement were observed during fretting tests at different cycles. For a normal load of 60 N, Figure 13b exposes a fretting loop with the same gross slip regime and its respective agreement with the wear track (see Figure 7c). When the maximum load of 80 N was applied, the fretting loop regime changed to a partial slip, as is observed in Figure 13c; the wear track observed in Figure 7e agrees well with this fretting regime [52]. Table 5 shows the dissipated energy (J/m), where sample S1 had the highest energies for all the normal loads applied. It was demonstrated that wear volume is linearly related to dissipated energy, but changes of tribochemistry in the contact resulted in a modification in the wear rate [60]. The sample S1 shows the lowest wear volume compared with sample S2, as can be seen in Figure 5c. This different behaviors between higher wear volume and lowest dissipated energy observed in sample S2 can be attributed to the tribolayer formatted during the fretting tests, the formation of carbon sp<sup>2</sup> structure [55], and its ability to lower the friction coefficient (<0.10) for carbon-based coatings [18,37,56], as already has been discussed previously.

**Table 5.** Dissipated energy (J/m), calculated from fretting tests at different normal loads.

Sample ID:	Normal Load		
	40 N	60 N	80 N
S1	$0.856 \times 10^{-3} \pm 1.21 \times 10^{-5}$	$0.705 \times 10^{-3} \pm 1.90 \times 10^{-5}$	$0.932 \times 10^{-3} \pm 1.06 \times 10^{-5}$
S2	$0.699 \times 10^{-3} \pm 0.70 \times 10^{-5}$	$0.633 \times 10^{-3} \pm 0.65 \times 10^{-5}$	$0.890 \times 10^{-3} \pm 1.04 \times 10^{-5}$

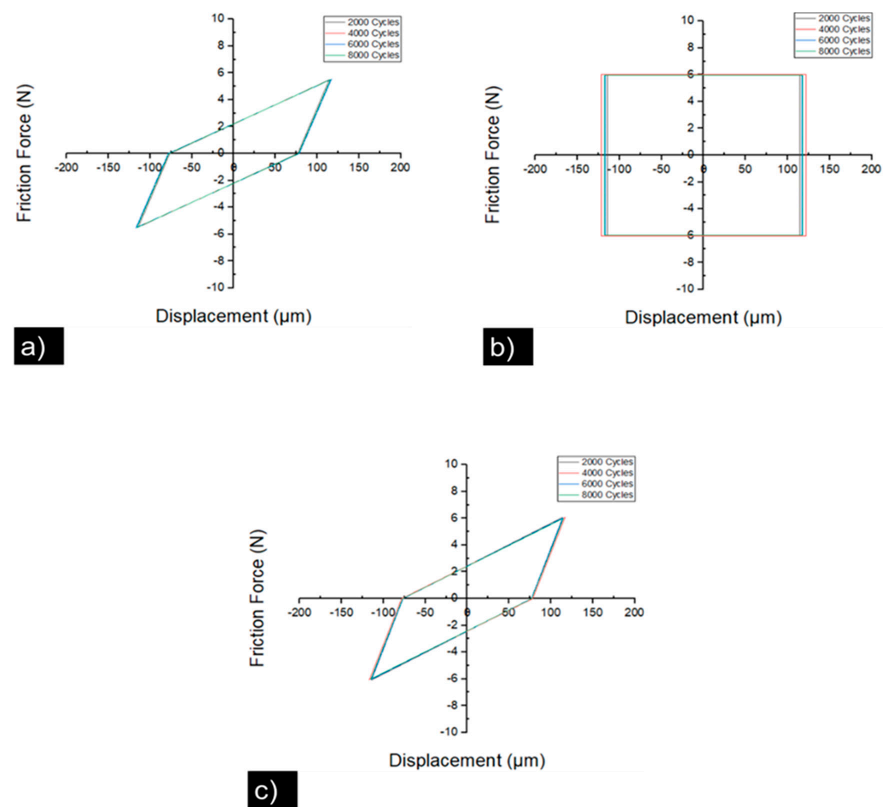


**Figure 12.** Friction force vs. displacement loops obtained at periodic intervals during the fretting test for sample S1, conducted at different loads: (a) 40 N, (b) 60 N, and (c) 80 N.

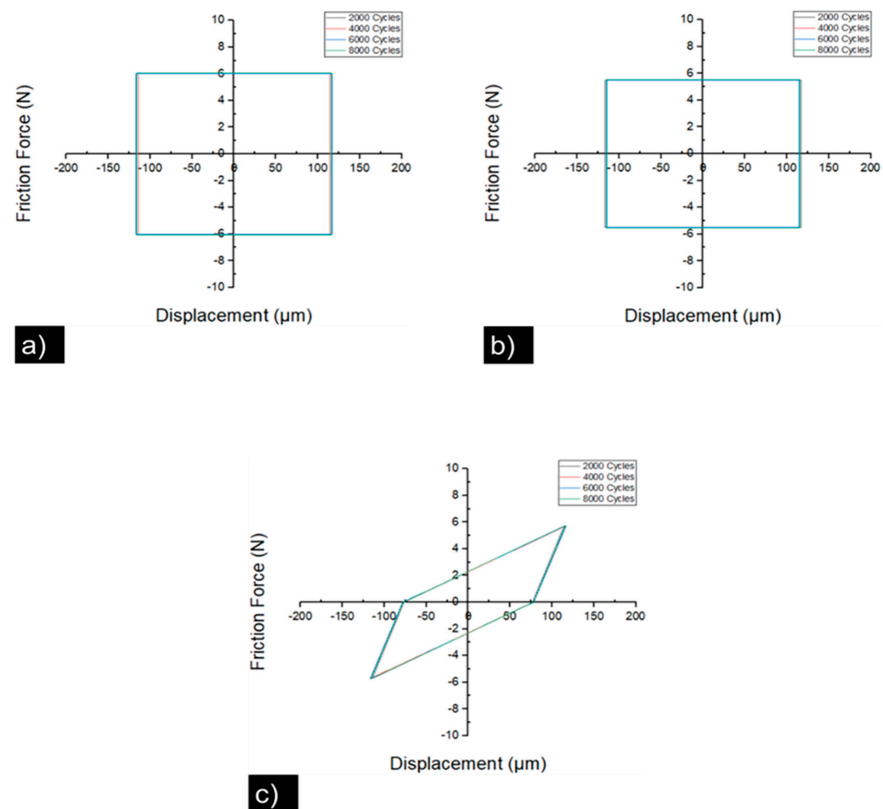


**Figure 13.** Friction force vs. displacement loops obtained at periodic intervals during the fretting test for sample S2, conducted at different loads: (a) 40 N, (b) 60 N, and (c) 80 N.

For the same applied displacement, a  $\Delta$  of 150  $\mu\text{m}$  was measured for different slip amplitudes  $2\delta$ , and these behaviors can be explained according to Vingsbo and Doderberg [61]. Here, the partial slip loop is related to a closed  $(\delta-F_f)$  cycle. In this regime, the contact area is divided into a sticking zone in the center of the contact and sliding zones at the edges, which can be observed in sample *S1* when normal loads of 40 and 80 N were applied during the fretting test (see Figure 12a,c) [61]. This behavior can be related to the wear track observed in Figure 6a,e. Alternatively, the same behavior was observed in the fretting loop (see Figure 13c) when a normal load of 80 N was applied in sample *S2*, and it agreed with the wear track observed in Figure 7e and with the absence of transfer material from the  $\text{CN}_x$  layer to the  $\text{Al}_2\text{O}_3$  ball, as can be seen in Figure 9f. On the other hand, in the gross slip regime, all the  $(\delta-F_f)$  cycles were quasi-rectangular loops (see Figure 13a,b). In this regime, there were higher displacement amplitudes. The sticking zone no longer existed and the whole contact was under full reciprocating sliding [61]. As can be seen, this behavior corresponded with the wear track shown in Figure 7a,c.

Experimental loops usually do not match well with the idealized shape, due to wear conditions and calculations not being simple [61]. Variables such as normal force  $F$ , friction force  $F_f$ , and the micro-slip at point in contact  $\delta$  affect the obtention of fretting loops. Then, to overcome these problems, tribometers are equipped with a force transducer combine with force actuators to measure the contact load during the fretting test [61]. In the fretting loop calculations, the tangential contact stiffness is defined by slope of the partial slip regime; however, this partial slip and contact interface is considered the most difficult variable to measure during the fretting testing. So, the slip amplitude  $\delta_0$  at each contact point is unknown during the fretting test, and sometimes this measurement is extrapolated from the displacement amplitude  $2\delta$  [61]. In other cases, slip amplitude measurements are performed between two reference points relatively far away from the contact. Finally, in some cases, the measurements were made between the specimen fixtures or directly from the displacement applied on the actuators [61]. In this study, these measurements were limited due to the configuration of the tribometer; nonetheless, fretting loops were obtained according to these implications.

#### 4. Conclusions

The CrAl/CrAlN and CrAl/CrAlN-(a-CN<sub>x</sub>) coatings were successfully deposited by the HIPIMS technique. The following conclusions can be summarized:

XRD characterization showed a cubic structure and orientations of (111), (200), (220), and (222) for CrAl/CrAlN coatings in samples *S1* and *S2*. FE-SEM analysis confirmed a glass-like morphology in the CrAl layer and in the (a-CN<sub>x</sub>) top layer, while the CrAlN layers exhibited a columnar morphology. This morphology made a difference in  $R_a$  values for sample *S1* compared to *S2* ( $0.03628 \mu\text{m} \pm 0.0058$  and  $0.02636 \mu\text{m} \pm 0.0055$ , respectively). Chemical composition confirms the presence of Cr and Al into the CrAl/CrAlN and CrAl/CrAlN-(a-CN<sub>x</sub>) multilayers.

Nanoindentation results showed a higher hardness in sample *S1* compared to sample *S2*; however, sample *S2* with the (a-CN<sub>x</sub>) top layer increased the absorption energy capacity and its mechanical potential energy stored, represented by the elastic recovery values. Moreover, sample *S2* showed the higher value for tribology aptness for the (H/E) relation, as well as resistance to plastic deformation by the  $(H^3/E^2)$  ratio.

Nano scratch test results on sample *S1* show the highest adhesion resistance and highest adhesive energy values, corresponding with the main coefficient of friction during the test and agreeing well with the higher values of the energy dissipated during the nanoindentation test, as well as its major architecture periodicity ( $1.5 \pm 0.06 \mu\text{m}$  in thickness).

Sample *S2* showed lower CoF values during fretting tests, due to the interaction of the a-CN<sub>x</sub> top layer with the counterbody and its capacity to form a tribolayer; the transfer material to the ball was confirmed by Raman spectroscopy. The Raman spectra subtracted from worn surfaces during the fretting test and the (D)/I(G) ratio showed an increase in the I(D)/I(G) ratio for sample *S2* tested at 40 N and 60 N, attributed to the formation of carbon

sp<sup>2</sup> structure (i.e., graphite-like structure) beneficial to low-friction coefficients (<0.10) for carbon-based coatings.

The CrAl/CrAlN and CrAl/CrAlN-(a-CN<sub>x</sub>) multilayers with thicknesses of  $1.5 \pm 0.06$  and  $1.2 \pm 0.05$  μm, respectively, proposed in this investigation improved the mechanical and tribological property behavior of the AISI A11 steel substrate and can be used as a potential protective surface for forms of moving parts such as gears, cutting tools, and shafts used in engines. Further studies must be done around plasma species characterization through optical emission spectroscopy (OES) and its comparison between sectioned targets with the alloyed target Cr-Al (0.50:0.50).

**Author Contributions:** C.J.M.-G.: methodology, investigation, writing—original draft. M.F.F.-J.: formal analysis, project administration. D.I.B.-B.: formal analysis, data curation, O.J.-A.: resources, supervision, writing—review and editing. M.F.-M.: resources, supervision, writing—review and editing. All authors have read and agreed to the published version of the manuscript.

**Funding:** This research was funded by Universidad de Guadalajara and Consejo Nacional de Ciencia y Tecnología (CONACYT), Frontiers of Science Program (Project 1103).

**Institutional Review Board Statement:** Not applicable.

**Informed Consent Statement:** Not applicable.

**Data Availability Statement:** Not applicable.

**Acknowledgments:** Cecilio J. Martínez-Gonzalez wants to thank the Programa de Doctorado en Ciencia de Materiales, Centro Universitario de Ciencias Exactas e Ingenierías (CUCEI), and the Maestría en Ciencia e Ingeniería de los Materiales, Universidad Autónoma de Zacatecas.

**Conflicts of Interest:** The authors declare no conflict of interest.

## References

1. Ding, X.Z.; Zeng, X.T.; Liu, Y.C.; Fang, F.Z.; Lim, G.C. Cr<sub>1-x</sub>Al<sub>x</sub>N coatings deposited by lateral rotating cathode arc for high speed machining applications. *Thin Solid Film.* **2008**, *516*, 1710–1715. [[CrossRef](#)]
2. Wang, L.; Zhang, G.; Wood, R.J.K.; Wang, S.C.; Xue, Q. Fabrication of CrAlN nanocomposite films with high hardness and excellent anti-wear performance for gear application. *Surf. Coat. Technol.* **2010**, *204*, 3517–3524. [[CrossRef](#)]
3. Tang, J.F.; Lin, C.Y.; Yang, F.C.; Chang, C.L. Influence of nitrogen content and bias voltage on residual stress and the tribological and mechanical properties of CrAlN films. *Coatings* **2020**, *10*, 546. [[CrossRef](#)]
4. Berg, G.; Friedrich, C.; Broszeit, E.; Berger, C. Development of chromium nitride coatings substituting titanium nitride. *Surf. Coat. Technol.* **1996**, *86*, 184–191. [[CrossRef](#)]
5. Khamseh, S.; Nose, M.; Kawabata, T.; Saiki, A.; Matsuda, K.; Terayama, K.; Ikeno, S. Effect of deposition conditions on the structure and properties of CrAlN films prepared by pulsed DC reactive sputtering in FTS mode at high Al content. *Mater. Trans.* **2008**, *49*, 2082–2090. [[CrossRef](#)]
6. Khamseh, S.; Nose, M.; Ueda, S.; Kawabata, T.; Nagae, T.; Matsuda, K.; Ikeno, S. Nanostructured CrAlN Films Prepared at Different Pulse Widths by Pulsed DC Reactive Sputtering in Facing Target Type System. *Mater. Trans.* **2008**, *49*, 0810100573. [[CrossRef](#)]
7. Nouveau, C.; Tlili, B.; Aknouche, H.; Benlatreche, Y.; Patel, B. Comparison of CrAlN layers obtained with one (CrAl) or two targets (Cr and Al) by magnetron sputtering. *Thin Solid Film.* **2012**, *520*, 2932–2937. [[CrossRef](#)]
8. Tsai, S.H.; Duh, J.G. Microstructure and Corrosion Properties of Multilayered CrAlN/SiN<sub>x</sub> Coatings. *J. Electrochem. Soc.* **2010**, *157*, K89. [[CrossRef](#)]
9. Ipaz, L.; Aperador, W.; Caicedo, J.; Esteve, J.; Zambrano, G. A Practical Application of X-ray Spectroscopy in Ti-Al-N and Cr-Al-N Thin Films. In *X-ray Spectroscopy*; InTech: Shanghai, China, 2012. [[CrossRef](#)]
10. Kaouther, K.; Hafedh, D.; Lassaad, Z.; Ahmed, B.C.L. Mechanical Characterization of CrN/CrAlN Multilayer Coatings Deposited by Magnetron Sputtering System. *J. Mater. Eng. Perform.* **2015**, *24*, 4077–4082. [[CrossRef](#)]
11. Paulitsch, J.; Schenkel, M.; Zufraß, T.; Mayrhofer, P.H.; Münz, W.D. Structure and properties of high power impulse magnetron sputtering and DC magnetron sputtering CrN and TiN films deposited in an industrial scale unit. *Thin Solid Film.* **2010**, *518*, 5558–5564. [[CrossRef](#)]
12. Bobzin, K.; Brögelmann, T.; Kruppe, N.C.; Engels, M.; Von Keudell, A.; Hecimovic, A.; Ludwig, A.; Grochla, D.; Banko, L. Fundamental study of an industrial reactive HPPMS (Cr, Al)N process. *J. Appl. Phys.* **2017**, *122*, 015302. [[CrossRef](#)]
13. Wu, Z.; Cheng, Z.; Zhang, H.; Xu, Z.; Wang, Y.; Zhou, F. Electrochemical and Tribological Properties of CrAlN, TiAlN, and CrTiN Coatings in Water-Based Cutting Fluid. *J. Mater. Eng. Perform.* **2020**, *29*, 2153–2163. [[CrossRef](#)]

14. Wang, X.; Kwon, P.Y.; Schrock, D.; Kim, D. Friction coefficient and sliding wear of AlTiN coating under various lubrication conditions. *Wear* **2013**, *304*, 67–76. [[CrossRef](#)]
15. Liu, D.; Ma, H.; Li, H.; Liang, Y. Structure, phase transformation and corrosion resistance of CrAlN/CN<sub>x</sub> composite multilayer films in NaCl aqueous solution. *Ceram. Int.* **2019**, *45*, 24446–24452. [[CrossRef](#)]
16. Tillmann, W.; Dias, N.F.L.; Stangier, D. Tribo-mechanical properties of CrC/a-C thin films sequentially deposited by HiPIMS and mfMS. *Surf. Coat. Technol.* **2018**, *335*, 173–180. [[CrossRef](#)]
17. Bakoglidis, K.D.; Schmidt, S.; Greczynski, G.; Hultman, L. Improved adhesion of carbon nitride coatings on steel substrates using metal HiPIMS pretreatments. *Surf. Coat. Technol.* **2016**, *302*, 454–462. [[CrossRef](#)]
18. Bakoglidis, K.D.; Schmidt, S.; Garbrecht, M.; Ivanov, I.G.; Jensen, J.; Greczynski, G.; Hultman, L. Low-temperature growth of low friction wear-resistant amorphous carbon nitride thin films by mid-frequency, high power impulse, and direct current magnetron sputtering. *J. Vac. Sci. Technol. A Vac. Surf. Film.* **2015**, *33*, 05E112. [[CrossRef](#)]
19. Bakoglidis, K.D.; Glenat, H.; Greczynski, G.; Schmidt, S.; Grillo, S.; Hultman, L.; Broitman, E. Comparative study of macro- and microtribological properties of carbon nitride thin films deposited by HiPIMS. *Wear* **2017**, *370–371*, 1–8. [[CrossRef](#)]
20. Terek, P.; Kukuruzović, D.; Kovačević, L.; Miletić, A.; Terek, V.; Škorić, B.; Panjan, P.; Čekada, M. The Influence of CrAlN Coating Chemical Composition on Soldering Resistance in Contact with Al-Si-Cu Alloy. *Mater. Proc.* **2020**, *2*, 28. [[CrossRef](#)]
21. Oliver, W.C.; Pharr, G.M. An improved technique for determining hardness and elastic modulus using load and displacement sensing indentation experiments. *J. Mater. Res.* **1992**, *7*, 1564–1583. [[CrossRef](#)]
22. Chang, S.Y.; Huang, Y.C. Analyses of interface adhesion between porous SiO<sub>2</sub> low-k film and SiC/SiN layers by nanoindentation and nanoscratch tests. *Microelectron. Eng.* **2007**, *84*, 319–327. [[CrossRef](#)]
23. Chang, S.-Y.; Lee, Y.-S.; Lu, C.-L. Effect of Plasma Treatments on the Interface Chemistry and Adhesion Strength Between Cu Metallization and SiCN Etch Stop Layer. *J. Electrochem. Soc.* **2007**, *154*, D241. [[CrossRef](#)]
24. Huang, Y.C.; Chang, S.Y.; Chang, C.H. Effect of residual stresses on mechanical properties and interface adhesion strength of SiN thin films. *Thin Solid Film.* **2009**, *517*, 4857–4861. [[CrossRef](#)]
25. Wang, Q.; Zhou, F.; Yan, J. Evaluating mechanical properties and crack resistance of CrN, CrTiN, CrAlN and CrTiAlN coatings by nanoindentation and scratch tests. *Surf. Coat. Technol.* **2016**, *285*, 203–213. [[CrossRef](#)]
26. Mayrhofer, P.H.; Music, D.; Reeswinkel, T.; Fuß, H.G.; Schneider, J.M. Structure, elastic properties and phase stability of Cr<sub>1-x</sub>Al<sub>x</sub>N. *Acta Mater.* **2008**, *56*, 2469–2475. [[CrossRef](#)]
27. Champi, A.; Lacerda, R.G.; Marques, F.C. Thermomechanical properties of the amorphous carbon nitride thin films. *Microelectron. J.* **2003**, *34*, 553–555. [[CrossRef](#)]
28. Dong, H.; Oganov, A.R.; Zhu, Q.; Qian, G.R. The phase diagram and hardness of carbon nitrides. *Sci. Rep.* **2015**, *5*, 9870. [[CrossRef](#)]
29. Liu, X.L.; Li, Z.H.; Xiao, Q.; Yang, W.B.; Chen, D.Y. Fretting Wear of Co-Cr-Mo Alloys at Elevated Temperatures. *J. Mater. Eng. Perform.* **2020**, *29*, 7499–7510. [[CrossRef](#)]
30. Vincent, L.; Berthier, Y.; Godet, M. *Testing Methods in Fretting Fatigue: A Critical Appraisal*; ASTM International: West Conshohocken, PA, USA, 1992; Volume 1159, pp. 33–48.
31. Panjan, P. Industrial applications of CrN (PVD) coatings, deposited at high and low temperatures. *Surf. Coat. Technol.* **1997**, *97*, 182–191.
32. Kong, J.Z.; Hou, T.J.; Wang, Q.Z.; Yin, L.; Zhou, F.; Zhou, Z.F.; Li, L.K.Y. Influence of titanium or aluminum doping on the electrochemical properties of CrN coatings in artificial seawater. *Surf. Coat. Technol.* **2016**, *307*, 118–124. [[CrossRef](#)]
33. Quintero, O.M.S.; Chaparro, W.A.; Ipaz, L.; Barco, J.E.S.; Beltrán, F.E.; Zambrano, G. Influence of the microstructure on the electrochemical properties of Al-Cr-N coatings deposited by Co-Sputtering method from a Cr-Al binary target. *Mater. Res.* **2013**, *16*, 204–214. [[CrossRef](#)]
34. Baseri, N.A.; Mohammadi, M.; Ghatee, M.; Abassi-Firouzjah, M.; Elmkhah, H. The effect of duty cycle on the mechanical and electrochemical corrosion properties of multilayer CrN/CrAlN coatings produced by cathodic arc evaporation. *Surf. Eng.* **2021**, *37*, 253–262. [[CrossRef](#)]
35. Lv, Y.; Ji, L.; Liu, X.; Li, H.; Zhou, H.; Chen, J. The structure and properties of CrAlN films deposited by mid-frequency unbalanced magnetron sputtering at different substrate bias duty cycles. *Surf. Coat. Technol.* **2012**, *206*, 3961–3969. [[CrossRef](#)]
36. Mohammadpour, E.; Jiang, Z.T.; Altarawneh, M.; Mondinos, N.; Rahman, M.M.; Lim, H.N.; Huang, N.M.; Xie, Z.; Zhou, Z.F.; Dlugogorski, B.Z. Experimental and predicted mechanical properties of Cr<sub>1-x</sub>Al<sub>x</sub>N thin films, at high temperatures, incorporating in situ synchrotron radiation X-ray diffraction and computational modelling. *RSC Adv.* **2017**, *7*, 22094–22104. [[CrossRef](#)]
37. Zheng, X.H.; Yang, F.E.; Chen, L.; Chen, Z.L.; Song, R.G.; Zhang, X.H. Microstructure and mechanical properties of a-CN<sub>x</sub> films prepared by bias voltage assisted PLD with carbon nitride target. *Surf. Coat. Technol.* **2014**, *258*, 716–721. [[CrossRef](#)]
38. Ferrari, A.C.; Rodil, S.E.; Robertson, J. Interpretation of infrared and Raman spectra of amorphous carbon nitrides. *Phys. Rev. B* **2003**, *67*, 155306. [[CrossRef](#)]
39. Ferrari, A.; Robertson, J. Interpretation of Raman spectra of disordered and amorphous carbon. *Phys. Rev. B—Condens. Matter Mater. Phys.* **2000**, *61*, 14095–14107. [[CrossRef](#)]
40. Zhao, Z.; Miao, Q.; Liang, W.; Xia, J.; Lin, H.; Qi, Y.; Zuo, S. Effect of CrAl interlayer on adhesion strength of CrAlN coating. *Surf. Eng.* **2020**, *36*, 438–446. [[CrossRef](#)]

41. Pérez-Alvarez, J.; Flores-Jiménez, M.; Rivera-Tello, C.D.; Suárez-Martínez, R.; Jimenez, O.; Flores-Cova, L.; Flores, M. Effect of a-CN<sub>x</sub> top layer on the electrochemical properties of Ta<sub>2</sub>N/Ta multilayers obtained by HIPIMS. *Mater. Lett.* **2020**, *278*, 128454. [[CrossRef](#)]
42. Zhou, F.; Adachi, K.; Kato, K. Comparisons of tribological property of a-C, a-CN<sub>x</sub> and BCN coatings sliding against SiC balls in water. *Surf. Coat. Technol.* **2006**, *200*, 4471–4478. [[CrossRef](#)]
43. Laegreid, N.; Wehner, G.K. Sputtering yields of metals for ar<sup>+</sup> and ne<sup>+</sup> ions with energies from 50 to 600 eV. *J. Appl. Phys.* **1961**, *32*, 365–369. [[CrossRef](#)]
44. Lv, F.; Wen, S.P.; Zong, R.L.; Zeng, F.; Gao, Y.; Pan, F. Nanoindentation study of amorphous-Co<sub>79</sub>Zr<sub>13</sub>Nb<sub>8</sub>/Cr multilayers. *Surf. Coat. Technol.* **2008**, *202*, 3239–3245. [[CrossRef](#)]
45. Horwat, D.; Jimenez-Pique, E.; Pierson, J.F.; Migot, S.; Dehmas, M.; Anglada, M. High hardness, low Young's modulus and low friction of nanocrystalline ZrW<sub>2</sub> Laves phase and Zr<sub>1-x</sub>W<sub>x</sub> thin films. *J. Phys. Chem. Solids* **2012**, *73*, 554–558. [[CrossRef](#)]
46. Kataria, S.; Kumar, N.; Dash, S.; Ramaseshan, R.; Tyagi, A.K. Evolution of deformation and friction during multimode scratch test on TiN coated D9 steel. *Surf. Coat. Technol.* **2010**, *205*, 922–927. [[CrossRef](#)]
47. Khelifi, K.; Ben Cheikh Larbi, A. Investigation of adhesion of PVD coatings using various approaches. *Surf. Eng.* **2013**, *29*, 555–560. [[CrossRef](#)]
48. Kim, K.H.; Han, D.S.; Kim, S.K. Adhesion properties of arc ion-plated TiN coatings with WC particle size, Co content and surface roughness. *Surf. Coat. Technol.* **2003**, *163–164*, 605–610. [[CrossRef](#)]
49. Yang, F.; Yang, S.; Chang, X.; Yang, W.; Song, R. Surface & Coatings Technology Microstructure and properties of DLC/CN<sub>x</sub> films with different CN<sub>x</sub> sublayer thicknesses. *Surf. Coat. Technol.* **2019**, *374*, 418–423. [[CrossRef](#)]
50. Shima, M.; Okado, J.; McColl, I.R.; Waterhouse, R.B.; Hasegawa, T.; Kasaya, M. The influence of substrate material and hardness on the fretting behaviour of TiN. *Wear* **1999**, *225–229*, 38–45. [[CrossRef](#)]
51. Zhang, D.K.; Ge, S.R.; Qiang, Y.H. Research on the fatigue and fracture behavior due to the fretting wear of steel wire in hoisting rope. *Wear* **2003**, *255*, 1233–1237. [[CrossRef](#)]
52. Ramesh, R.; Gnanamoorthy, R. Development of a fretting wear test rig and preliminary studies for understanding the fretting wear properties of steels. *Mater. Des.* **2006**, *27*, 141–146. [[CrossRef](#)]
53. Endrino, J.L.; Fox-Rabinovich, G.S.; Reiter, A.; Veldhuis, S.V.; Galindo, R.E.; Albella, J.M.; Marco, J.F. Oxidation tuning in AlCrN coatings. *Surf. Coat. Technol.* **2007**, *201*, 4505–4511. [[CrossRef](#)]
54. Rebelo de Figueiredo, M.; Bergmann, C.; Ganser, C.; Teichert, C.; Kukla, C.; Mitterer, C. Adhesion tendency of polymers to hard coatings. *Int. Polym. Process.* **2013**, *28*, 415–420. [[CrossRef](#)]
55. Wang, P.; Zhang, W.; Diao, D. Low friction of graphene nanocrystallite embedded carbon nitride coatings prepared with MCECR plasma sputtering. *Surf. Coat. Technol.* **2017**, *332*, 153–160. [[CrossRef](#)]
56. Wang, P.; Adachi, K. Low frictions of self-mated CN<sub>x</sub> coatings in dry and humid inert gas environments. *Surf. Coat. Technol.* **2014**, *258*, 1137–1144. [[CrossRef](#)]
57. A Global Methodology to Quantify Fretting Damage | Request PDF, (n.d.). Available online: [https://www.researchgate.net/publication/289362712\\_A\\_global\\_methodology\\_to\\_quantify\\_fretting\\_damage](https://www.researchgate.net/publication/289362712_A_global_methodology_to_quantify_fretting_damage) (accessed on 20 July 2023).
58. Varenberg, M.; Etsion, I.; Halperin, G. Slip index: A new unified approach to fretting. *Tribol. Lett.* **2004**, *17*, 569–573. [[CrossRef](#)]
59. Chaudhry, V.; Kailas, S.V. Fretting studies on self-mated stainless steel and chromium carbide coated surfaces under controlled environment conditions. *Wear* **2013**, *301*, 524–539. [[CrossRef](#)]
60. Huq, M.Z.; Celis, J.-P. Expressing wear rate in sliding contacts based on dissipated energy. *Wear* **2002**, *252*, 375–383. [[CrossRef](#)]
61. Vingsbo, O.; Söderberg, S. On fretting maps. *Wear* **1988**, *126*, 131–147. [[CrossRef](#)]

**Disclaimer/Publisher's Note:** The statements, opinions and data contained in all publications are solely those of the individual author(s) and contributor(s) and not of MDPI and/or the editor(s). MDPI and/or the editor(s) disclaim responsibility for any injury to people or property resulting from any ideas, methods, instructions or products referred to in the content.